# SMALL DISTURBANCE NAVIER-STOKES INVESTIGATIONS OF FIGHTER-TYPE-DELTA-WING PITCHING OSCILLATIONS

**Alexander Pechloff** *
**Technische Universität München, Boltzmannstr. 15, D-85748 Garching, Germany**
**alexander.pechloff@alumni.tum.de**

**Keywords:** *small disturbance Navier-Stokes equations, computational fluid dynamics, aeroelasticity*

## Abstract

*The small disturbance Navier-Stokes method FLM-SD.NS developed at Technische Universität München was shown to be both an efficient and yet accurate means of rendering the unsteady aerodynamic loading required by transonic aeroelastic analysis. Complementing past investigations, FLM-SD.NS computations of a fighter-type delta-wing undergoing harmonic pitching-oscillations are presented. The considered cases respectively feature a shockless flow-topology, leading-edge vortex formation, and a medium-strength shock. Overall, the unsteady aerodynamic loading is again obtained in good agreement with dynamically fully nonlinear predictions provided by the comparative Reynolds-averaged Navier-Stokes method FLM-NS. Reductions in computation time, up to half an order of magnitude, in relation to FLM-NS are observed. The known limitations of the small disturbance approach become apparent for the leading-edge-vortex case, in which higher-order harmonics are far less negligible in the flow's response to the excitation. Despite featuring substantially differing flow-topologies, the degree of dynamic stability exhibited by the fighter-type delta-wing in the leading-edge-vortex case is ascertained to be nearly equal to the instance in the shockless case. Contrarily, the degree of dynamic stability exhibited in the medium-strength-shock case emerges greatly reduced with respect to the shockless case. A comparison to both small-disturbance and dynamically-fully-nonlinear Euler results, respectively, rendered by FLM-SDEu and FLM-Eu, is also made. It primarily shows that for the more intricate flow-topologies the viscous consideration substantially improves on the inviscid prediction of the global load coefficients' zeroth-harmonic, yet to a lesser extent on their first-harmonic. For each case, however, the degree of dynamic stability determined with FLM-SDEu / FLM-Eu is quite similar to the FLM-SD.NS / FLM-NS-assessed counterpart.*

## Nomenclature

| | | |
|---|---|---|
| $A$ | = | semi-span planform area, $\int_0^s c\,dy$ |
| AR | = | semi-span aspect ratio, $s^2/A$ |
| $c$ | = | local chord length, $c(y/s)$ |
| $c_{av}$ | = | average chord length, $A/s$ |
| $c_L$ | = | lift coefficient, dimensional lift normalized with $\check{\rho}_\infty \lvert\check{\mathbf{v}}_\infty\rvert^2 \check{A}/2$ |
| $c_M$ | = | moment coefficient, dimensional moment respective to the pitch axis normalized with $\check{\rho}_\infty \lvert\check{\mathbf{v}}_\infty\rvert^2 \check{A}\check{c}_\mu/2$ (greater than 0: tail-heavy moment/pitch up) |
| $c_p$ | = | pressure coefficient |
| $c_{p,crit}$ | = | critical pressure coefficient, $c_p(Ma_\infty)$ at $Ma = 1.0$ |
| $c_r$ | = | root chord length, $c(0)$ |
| $c_t$ | = | tip chord length, $c(1)$ |
| $c_\mu$ | = | reference chord length, $\int_0^s c^2\,dy/A$ |

* Dipl.-Ing. (Univ.), Research Engineer, Institute for Aero- and Astronautics

| | | |
|---|---|---|
| $d^+$ | = | sublayer-scaled distance of the first offbody grid plane |
| $f$ | = | oscillation frequency |
| $Im$ | = | imaginary part |
| $k_{red}$ | = | reduced oscillation frequency, $2\pi\check{f}\check{L}\sqrt{\check{\rho}_\infty}/(Ma_\infty\sqrt{\gamma\check{p}_\infty})$ |
| $L$ | = | reference length of the geometric nondimensionalization |
| $Ma$ | = | local Mach number |
| $Ma_\infty$ | = | freestream Mach number, $\lvert\check{\mathbf{v}}_\infty\rvert\sqrt{\check{\rho}_\infty}/\sqrt{\gamma\check{p}_\infty}$ |
| $p_\infty$ | = | freestream static pressure |
| $Pr$ | = | Prandtl number |
| $Pr_t$ | = | turbulent Prandtl number |
| $Re$ | = | real part |
| $Re_\infty$ | = | freestream Reynolds number, $\check{\rho}_\infty\lvert\check{\mathbf{v}}_\infty\rvert\check{c}_{av}/\check{\mu}_\infty$ |
| $s$ | = | semispan length |
| $T_\infty$ | = | freestream static temperature |
| $t$ | = | time |
| $t_{CPU}^{method}$ | = | Institute of Fluid Mechanics method computation time |
| $\lvert\mathbf{v}_\infty\rvert$ | = | magnitude of the freestream velocity vector |
| $x$ | = | span-station-local chordwise coordinate, $x(y/s)$ (0: leading edge, $c$: trailing edge) |
| $x, y, z$ | = | global Cartesian coordinates |
| $x_d$ | = | $x$ of a wing section's maximum thickness |
| $x_p, z_p$ | = | global pitch axis coordinates |
| $y$ | = | semi-span coordinate (0: root, $s$: tip) |
| $\alpha$ | = | incidence angle |
| $\gamma$ | = | ratio of specific heats |
| $\Delta$ | = | difference between lower- and upper-surface value, $\Delta(x/c)$; for example, $\Delta c_p = c_{p,lower} - c_{p,upper}$ |
| $\zeta_{CPU}$ | = | ratio of computation times, $\check{t}_{CPU}^{NS}/\check{t}_{CPU}^{SD.NS}$ |
| $\lambda$ | = | taper ratio, $c_t/c_r$ |
| $\mu$ | = | molecular viscosity, governed by Sutherland's law |
| $\mu_\infty$ | = | freestream molecular viscosity, $\mu(T_\infty)$ |
| $\rho_\infty$ | = | freestream density |
| $\tau_s$ | = | characteristic time, $\check{t}Ma_\infty\sqrt{\gamma\check{p}_\infty}/(\check{L}\sqrt{\check{\rho}_\infty})$ |
| $\chi$ | | generalized load coefficient, $\chi \in \{c_p, c_L, c_M\}$ |

*Superscripts*

| | | |
|---|---|---|
| 0 | = | zeroth harmonic |
| 1 | = | first harmonic |
| 2, 3 | = | higher harmonics (second, third) |
| $\bar{}$ | = | time-invariant mean |
| $\tilde{}$ | = | periodic perturbation |
| $\hat{}$ | = | perturbation amplitude |
| $\check{}$ | = | dimensional |

## 1 Introduction

In the transonic speed range, production analysis of an aircraft's dynamic aeroelastic behavior requires a computational fluid dynamics (CFD) method that can efficiently supply the unsteady aerodynamic structural loading, while accurately accounting for both compressibility and viscosity effects [13]. Research conducted at the former Institute for Fluid Mechanics (FLM)[†] of the Technische Universität München has shown that a CFD method based on the small disturbance Navier-Stokes equations can satisfy these needs [9]: Under the premise of a predominantly dynamically-linear flowfield-response to a first-harmonic excitation, the amplitude of the organized unsteadiness, and thus the amplitude of the unsteady aerodynamic loading, can be extracted and computed directly in the frequency domain. As a result, the computational cost becomes merely a fraction of the one associated with the otherwise commonly employed time-domain Reynolds-averaged Navier-Stokes (RANS) approach, while retaining its fidelity to a high degree.

The small disturbance Navier-Stokes solution develops subject to a specified $k_{red}$ and ampli-

[†]The FLM was reconstituted as the Institute of Aerodynamics in December 2004 under Prof. Dr.-Ing. Nikolaus Adams, and subsequently renamed the Institute of Aerodynamics and Fluid Mechanics in December 2010.

tude surface deflection/deformation of the considered body's harmonic motion on basis of a reference (time-invariant mean) flowfield. The latter is a priori supplied by a steady-state RANS solution realized in a computational grid embedding the considered body at its zero-crossing (reference) position for the $Ma_\infty$, $Re_\infty$, and $\breve{\alpha}$ of interest. In addition to this reference grid, a second grid embedding the considered body at its upper-dead-center (extremum) position must be provided. It allows the required amplitude surface-deflection/deformation to be numerically extracted.

The application readiness of the realized incarnation, designated FLM-SD.NS, had been demonstrated through investigations on harmonic oscillations of both low- and high-aspect-ratio wings, as well as a rectangular-wing/nacelle configuration [11, 10, 3]. The accuracy and the achieved efficiency-gain had been assessed by comparing the FLM-SD.NS results and required computational time to those of the in-house RANS method FLM-NS. A reduction of computational time up to an order of magnitude was principally ascertained. An additional comparison with both the in-house small disturbance Euler method FLM-SDEu [5, 16, 14] and its dynamically-fully-nonlinear time-domain counterpart FLM-Eu highlighted the advantages of the viscous approach over the inviscid one. Within the FLM-SD.NS framework the perturbation amplitude of the eddy viscosity is fully accounted for by default.

Per se, the application of small disturbance Navier-Stokes methods to aircraft aeroelasticity is still in its infancy. As of 2012 only a few other endeavors have been made to appropriate established RANS methods as basis for complementary small disturbance Navier-Stokes incarnations. Notably, small disturbance Navier-Stokes methods based on Dassault Aviation's AETHER [6, 12], the French Aerospace Laboratory's elsA [7, 2], and the German Aerospace Center's TAU [17] have come into existence.

Next to the well established standard test cases employed in the FLM-CFD methods' validation, application-oriented cases of a fighter-type delta wing (FTDW) performing harmonic motions under high-Reynolds-number transonic flow conditions had been a research focus for many years at the FLM. Embodying the wing of a highly maneuverable aircraft, the flow around the FTDW remains shockless up to nearly sonic freestream Mach-numbers for moderate incidence-angles. High incidence-angles in combination with high subsonic freestream Mach-numbers, on the other hand, initiate a vortex close to the upper-surface leading-edge (LE). Designated the leading-edge vortex (LEV), it introduces considerable cross-flow velocities to the nearfield, augmenting the degree of suction the upper-surface is exposed to in return. Consequently, the resultant lift still increases over its moderate-incidence-angle counterparts at equal freestream Mach-number instead of collapsing, as typically observed for other wing geometries at high incidence-angles due to flow separation.

Primarily, inviscid investigations had been conducted for the FTDW, with FLM-SDEu / FLM-Eu employed to render the unsteady aerodynamic-loading induced by rigid-body pitching- and flap-oscillations, as well as elastic-eigenmode oscillations [16, 14]. To date, viscous investigations realized with FLM-SD.NS / FLM-NS were limited to the particular FTDW flap-oscillation cases [4]. Complementing these results, a series of pitching-oscillation cases based on those presented in [16] were novelly computed with FLM-SD.NS. The small disturbance accordant formulation of the Spalart-Allmaras (S/A) one-equation turbulence model [15] was employed. In the following, select cases are presented and discussed.

## 2 Numerical Method

FLM-SD.NS is a cell-centered structured finite volume method (multiblock capable) featuring a multigrid-accelerated implicit pseudotime-integration of the discretized small disturbance Navier-Stokes equations. Second-order spatial accuracy is given for smoothly stretched grids and regions of continuous flow, with the total variation diminishing condition yet satisfied at lo-

cations of discontinuity. Details on the numerical properties have been provided in [9, 3, 11, 10].

Investigating the harmonic pitching oscillations of the FTDW, all FLM-CFD methods consider the motion to be governed by

$$\begin{aligned} \breve{\alpha}(k_{red}\,\tau_s) &= \breve{\bar{\alpha}} + \breve{\tilde{\alpha}}(k_{red}\,\tau_s) \quad \text{with} \\ \breve{\tilde{\alpha}}(k_{red}\,\tau_s) &:= \breve{\alpha}\,\sin(k_{red}\,\tau_s) \end{aligned} \tag{1}$$

about the given pitch axis, with $\breve{\alpha}$, $\breve{\bar{\alpha}}$, and $k_{red}$ set through the individual test case.

For FLM-SD.NS the local unsteady load distribution normal to the wing's surface, embodied by $\bar{c}_p$, $\hat{c}_p$, as well as the resultant global loading, expressed by $\bar{c}_L$, $\hat{c}_L$ and $\bar{c}_M$, $\hat{c}_M$, are investigated. The latter are directly gained from the integration of the $\bar{c}_p$, $\hat{c}_p$ and $\bar{c}_f$, $\hat{c}_f$ distributions over the wing's reference position surface. If desired, time-dependent $c_p$, $c_L$, and $c_M$ evolutions can be gained by recomposite, that is,

$$\begin{aligned} \chi(k_{red}\,\tau_s)|_{SD.NS} &:= \bar{\chi} + \tilde{\chi}(k_{red}\,\tau_s) \text{ with} \\ \tilde{\chi}(k_{red}\,\tau_s) &= Re\hat{\chi}\,\sin(k_{red}\,\tau_s) \\ &+ Im\hat{\chi}\,\cos(k_{red}\,\tau_s)\,. \end{aligned} \tag{2}$$

An $Im\hat{\chi} > 0$ indicates a $\tilde{\chi}$ that leads the excitation, while complementarily a $Im\hat{\chi} < 0$ indicates a $\tilde{\chi}$ that lags the excitation [11]. In this context, the evaluation of the systemic energy transfer by $\tilde{c}_M$ over the course of a single period shows that for $\hat{\alpha} > 0$ the corresponding free pitching oscillation can be classified as unstable if $Im\hat{c}_M > 0$ or stable if $Im\hat{c}_M < 0$. This conforms, respectively, to a $\tilde{c}_M$ that either has an amplifying or a damping effect.

Typically, the FLM-SD.NS time-invariant mean and complex amplitude result – the load coefficients' zeroth and first harmonic – are compared to the particular instances yielding from the Fourier-analyzed FLM-NS time series of a periodic cycle. This not only allows FLM-SD.NS prediction-accuracy to be ascertained, but also the degree of dynamic nonlinearity inherent to the time-accurate flow response. The discrete evolution of $c_L$ and $c_M$ itself arises from the integration of the $c_p$ and $c_f$ distributions over the deflected wing's surface after each converged physical time step. For this purpose, the nomenclature of the FLM-SD.NS-computed load coefficients is brought into conformity with that common to the Fourier-analysis:

$$\chi^0|_{SD.NS} := \bar{\chi}, \qquad \chi^1|_{SD.NS} := \hat{\chi}. \tag{3}$$

Both FLM-NS and FLM-Eu render the unsteady aerodynamic loading with second-order accuracy in time. The globally used Cartesian coordinate system is set to originate from the wing's root LE at reference position. The $x$ (chordwise) direction runs positively toward the trailing edge (TE) and the $y$ (spanwise) direction runs positively toward the starboard tip, rendering the designated reference plane for $\breve{\alpha}$. The imposed motion is strictly longitudinal, that is, occurring about an axis parallel to the spanwise direction. Consequently, a semispan numerical treatment of the FTDW suffices, the starboard half being considered here.

## 3 Fighter Type Delta Wing

The clipped FTDW features a 53 deg swept LE, a 3 deg negatively-swept TE, and a supercritical section (round LE, sharp TE) which varies in both geometry and twist across the span (Fig. 1): Relative thickness reduces from 4.7% for the root section ($x_d/c_r = 0.49$) to 4.0% for the tip section ($x_d/c_t = 0.35$). The tip section exhibits an accrued twist of $-5$ deg respective the root section. In its semi-span instance ($\breve{L} := \breve{s} = 5.258$ m) the planform is trapezoidal, with $s := \breve{s}/\breve{L} = 1.0$ and $c_r := \breve{c}_r/\breve{L} = 1.615$ supplementing the sweep angles in the definition. Evidently, the planform of the FTDW is quite similar to the planform of the NASA Clipped Delta Wing (NCDW) [1], which had been employed in the three-dimensional validation of FLM-SD.NS [4, 11]. The FTDW's secondary geometric properties result to $\lambda = 0.146$, $A := \breve{A}/\breve{L}^2 = 0.926$, AR $= 1.080$, $c_{av} := \breve{c}_{av}/\breve{L} = 0.926$, and $c_\mu := \breve{c}_\mu/\breve{L} = 1.097$. The pitch axis resides at $x_p/c_r = 0.50$ and $z_p = 0.00$. Surface pressure distributions are evaluated at merely one in-

ner and one outer span station, $y_{s1} := y/s = 0.35$ and $y_{s2} = 0.75$, respectively.

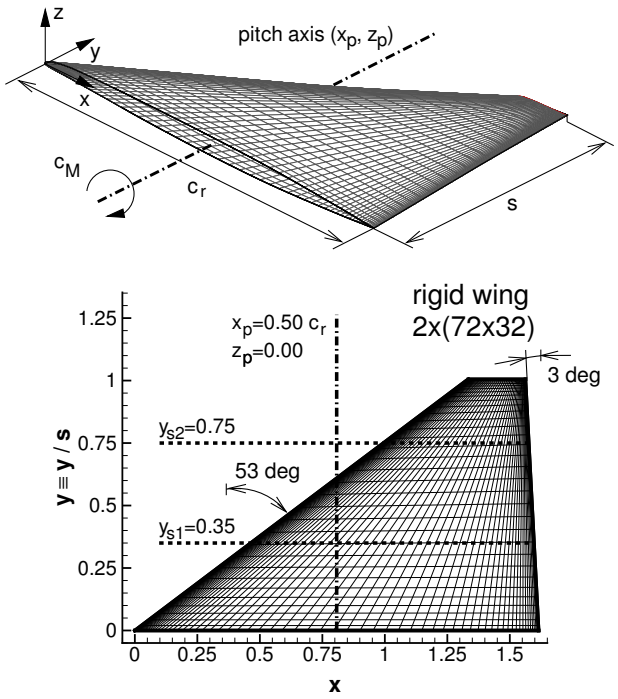


**Fig. 1** Composited spatial and planform view (surface grid with superimposed pitch axis and investigated span stations) of the rendered FTDW

Retaining the discretization established for the NCDW, 72 cells are hyperbolically distributed in chordwise and 32 cells Poisson-distributed in spanwise direction for a total of 2304 cells on each surface. Pertinent initial spacings at the LE and root section, as well as final spacings at the TE end tip section are adjusted from their NCDW-setting to accommodate the geometric differences, in particular the round LE. It is embedded (at reference position) in an elliptically smoothed two-block C-H-topology structured volume grid by way of a boundary-fitted curvilinear coordinate system. The far-field distances are set to $11 \times s$ in positive chordwise direction from the root LE, to $11 \times s$ in both positive and negative vertical ($z$) direction from the root TE, as well as to $5 \times s$ in spanwise direction respective the wing's lateral ($xz$) plane of symmetry. Evidently, the employed topology and far-field distances are chosen to be identical to those utilized by the NCDW volume grid. In contrast to it, each block now discretizes approximately one half of the numerically treated physical domain, as the embedded wing has no vertical plane of symmetry: The NCDW volume grid had been conveniently divided into physically-equal spatial parts by the $xy$ plane. The individual block is still associated with strictly one of the wing's surfaces, either the upper or lower. It discretizes the delimited volume with 96 cells in positive chordwise, 48 cells in spanwise, and 40 cells in wing surface normal direction, translating into 184320 cells per block or 368640 cells for the entire grid. Cells in wing surface normal direction are hyperbolically distributed, the distance of the first offbody grid plane being set to $1 \times 10^{-5} \times s$. For the considered high-Reynolds-number transonic flow this renders $d^+ < 5$ as required by the S/A turbulence model. The employed cell distributions and offbody distances are again chosen to be equal to those utilized by the NCDW volume grid. Regeneration of the volume grid for the amplitude-deflected surface grid and subsequent smoothing ultimately yields the desired extremum grid. Hence, its global properties are equivalent to those of the reference grid. Further details on grid construction and smoothing are given in [8].

From the multitude of computed dynamic test cases, results for a shockless case (P800510), an LEV case (P801010), and a medium-strength-shock case (P950510) are presented. Table 1 provides the computation parameters. For all cases, the values of the dimensional thermodynamic reference quantities complementing $\check{L}$ are $\check{p}_\infty = 101.3$ kPa, $\check{\rho}_\infty = 1.255$ kg/m$^3$, and $\check{T}_\infty = 288.15$ K, while also having $Re_\infty = 10.0 \times 10^6$, $\gamma = 1.4$, $Pr = 0.72$ (air), and $Pr_t = 0.90$ in common. The S/A one-equation turbulence model [15] is selected to provide eddy-viscosity closure. Test case P800510 will serve as baseline.

FLM-SD.NS computations of P800510 and P950510 employ a three-level V-symmetric multigrid cycle for acceleration. Per multigrid cycle dual pseudotime steps on the finest and coarsest grid level in combination with a single pseudotime step on the intermediary level (2/1/2)

| Case | $Ma_\infty$ | $\breve{\alpha}$, deg | $\breve{\alpha}$, deg | $k_{red}$ | $\breve{f}$, Hz |
|---|---|---|---|---|---|
| P800510 | 0.80 | 5.0 | 1.0 | 1.0 | 8.2 |
| P801010 | 0.80 | 10.0 | 1.0 | 1.0 | 8.2 |
| P950510 | 0.95 | 5.0 | 0.5 | 1.0 | 9.8 |

**Table 1** Computation parameters of the FTDW cases

are conducted. The NCDW computations [11] had established this setting to be well suited for efficiently converging solutions. It has become the quasi default setting, as permitted by the employed grid's actual multigrid-capability. A converged solution of the governing equations is assumed if the $L_2$-norm amplitude density residual, as normalized with its value after the first multigrid cycle, has dropped below $5.0 \times 10^{-4}$, terminating the computation.

For P801010, where an extensive region of LEV-induced near-surface cross-flow occurs in the supplied time-invariant mean flowfield, stability of the solution process could merely be achieved under the singlegrid setting and the so-called frozen eddy-viscosity approach: The amplitude S/A working variable is artificially kept at nil value throughout the entire domain, effectively eliminating the amplitude eddy-viscosity's contribution to the developing solution. Stability realized in this manner, however, comes at the expense of a turbulent closure diminished in its dynamic trait. Nevertheless, the localized limitation of the amplitude S/A working variable, first established in [11], is not explored in this context as an alternative remedy for solution instability. The precedingly specified abort criterion remains valid, however, revised in terms of the singlegrid cycle.

For the comparative FLM-NS computations three oscillation cycles suffice to achieve load coefficient periodicity, each discretized with 100 physical time intervals. This is equal to the treatment of the NCDW cases. Incremental grid deformation is again carried out through time-law-accordant inter- and extrapolation between the extremum and reference grid. Solution scheme settings are, respectively, identical to those of the corresponding FLM-SD.NS computation. All FLM-SD.NS / FLM-NS production-computations were conducted on a single 1.3 GHz Intel Itanium 2 processor of the Leibniz Rechenzentrum Linux cluster. The employed FLM-CFD method's machine code was generated from its serial implementation with the Intel Fortran Compiler for Linux.

Generally, the supplemental FLM-SDEu / FLM-Eu computations employ the same reference and extremum grid as the FLM-SD.NS / FLM-NS ones in order to retain spatial comparability. For P801010, however, the high resolution of the wing's near-field destabilized the inviscid solution process, as previously witnessed for the NCDW case 90D29 [11]. This necessitates the consideration of more Euler-typical grids, which are internally generated from the Navier-Stokes grids through elimination of every other cell edge. Ultimately, coarser grids of merely 46080 cells are rendered, with 576 cells constituting each surface. This poses a substantial reduction, respectively, by 88% and 75%. Nevertheless, the wing surface and near-field remain sufficiently resolved, with the distance of the first offbody grid plane only increasing to $3 \times 10^{-5} \times s$. Experimental data in regard to the considered test cases was not available. In the following, the load coefficients' real and imaginary parts are normalized with $\hat{\alpha} := \breve{\alpha}\pi/180$ deg.

## 4 Results and Discussion

### 4.1 Shockless Case

For $Ma_\infty = 0.80$, $Re_\infty = 10.0 \times 10^6$, and $\breve{\alpha} = 5.0$ deg the FLM-NS supplied time-invariant mean flowfield exhibits a highly localized supersonic region in proximity to the upper wing-surface, originating close to the LE. It extends from $y/s = 0.29$ to the tip, terminating without a shock. FLM-SD.NS-computed surface pressure distributions for P800510 are composited with their FLM-NS and FLM-SDEu / FLM-Eu counterparts in Fig. 2. Subsequently, the FLM-SD.NS result is briefly described.

For both the inner- and outer-span station, a

lower-surface maximum $c_p^0$-peak presents itself close to the LE, designating the local stagnation point. The strong acceleration around the LE toward the upper-surface then renders an equally distinct minimum $c_p^0$-peak, that is, the $c_p^0$ suction-peak, which apparently increases in absolute value from root to tip. Despite upper-surface $c_p^0$ falling below $c_{p,crit}$ significantly, the recompression toward the TE occurs continuously, as characteristic for a supercritical airfoil. Lower-surface flow remains entirely subsonic, with the rendered $c_p^0$-progression indicating an expansion that is sustained over the greater part of the local chord length, before again continuously recompressing toward equalization with the upper-surface $c_p^0$-progression at the TE. Integrating $\Delta c_p^0$ over the entire wing, a positive $c_L^0$ and marginally negative $c_M^0$ can be ascertained.

The $Re\,c_p^1$ progressions exhibit an upper-surface minimum-peak and a substantially diminished lower-surface maximum-peak, respectively, corresponding to the particular location of the $c_p^0$ suction-peak and the local stagnation point. For either span station the upper- and lower-surface $Re\,c_p^1$ progression are observed to intersect in close proximity to the TE, eventually equalizing there. Integrating $\Delta Re\,c_p^1$ over the entire wing, a positive $Re\,c_L^1$ and negative $Re\,c_M^1$ (pitch down) can be ascertained.

Inverse to the $Re\,c_p^1$ progressions, the $Im\,c_p^1$ progressions feature an upper-surface maximum-peak and a lower-surface minimum-peak, respectively, at the particular location of the $c_p^0$ suction-peak and the local stagnation point. For the inner-span station, the upper- and lower-surface $Im\,c_p^1$-progressions intersect slightly forward of the pertinent pitch-axis location, while intersecting farther upstream relative to the chord-length for the outer-span station. For either span station, upper-surface and lower-surface $Im\,c_p^1$ progress downstream, respectively, toward a minimum and maximum value, subsequently trending toward equalization at the TE. Integrating $\Delta Im\,c_p^1$ over the entire wing, a positive $Im\,c_L^1$ and negative $Im\,c_M^1$ (pitch down) can be ascertained.

For both span stations, FLM-SD.NS-computed $c_p^0$, $Re\,c_p^1$, and $Im\,c_p^1$ agree excellently with their FLM-NS counterparts. As expected, the small disturbance premise holds up very well for shockless transonic flow. Mild discrepancies are merely observed in the upper-surface $Re\,c_p^1$- and $Im\,c_p^1$-progressions, hinting at some higher-harmonic influence. The conformity between FLM-SD.NS and FLM-NS can be seen equal to that between FLM-SDEu and FLM-Eu. Overall, the viscous and inviscid progressions differ only marginally.

Considering the computed global load coefficients (Table 2), both $c_L^0$ and $Re\,c_L^1$ gained from FLM-SD.NS conform to their respective FLM-NS counterpart. In contrast, FLM-SD.NS-computed $Im\,c_L^1$ is rendered 4% lower than the FLM-NS-obtained instance. $Re\,c_L^1$ and $Im\,c_L^1$ are in the same order of magnitude. Both computations congruently predict a time-dependent $c_L$ that substantially leads the excitation.

| Method | $c_L^0$ | $Re\,c_L^1$ | $Im\,c_L^1$ |
|---|---|---|---|
| FLM-SD.NS | 0.214 | 3.481 | 1.987 |
| FLM-NS | 0.214 | 3.479 | 2.070 |
| FLM-SDEu | 0.219 | 3.609 | 2.073 |
| FLM-Eu | 0.220 | 3.613 | 2.182 |

| Method | $c_M^0$ | $Re\,c_M^1$ | $Im\,c_M^1$ |
|---|---|---|---|
| FLM-SD.NS | -0.005 | -0.246 | -1.001 |
| FLM-NS | -0.005 | -0.211 | -1.039 |
| FLM-SDEu | -0.006 | -0.295 | -1.065 |
| FLM-Eu | -0.007 | -0.256 | -1.118 |

**Table 2** Comparison of the global load coefficients for FTDW case P800510 ($Ma_\infty = 0.80$, $Re_\infty = 10.0 \times 10^6$, $\breve{\alpha} = 5.0$ deg, $\breve{\alpha} = 1.0$ deg, $k_{red} = 1.0$, $x_p/c_r = 0.50$)

FLM-SDEu-rendered $c_L^0$ is merely 2% higher than its FLM-SD.NS counterpart, while both $Re\,c_L^1$ and $Im\,c_L^1$ are 4% higher. In either case, the difference is accrued through the marginally wider lower- and upper-surface sectional local-load-coefficient progression ($c_p^0$, $Re\,c_p^1$, $Im\,c_p^1$) – thus respectively yielding a larger sectional con-

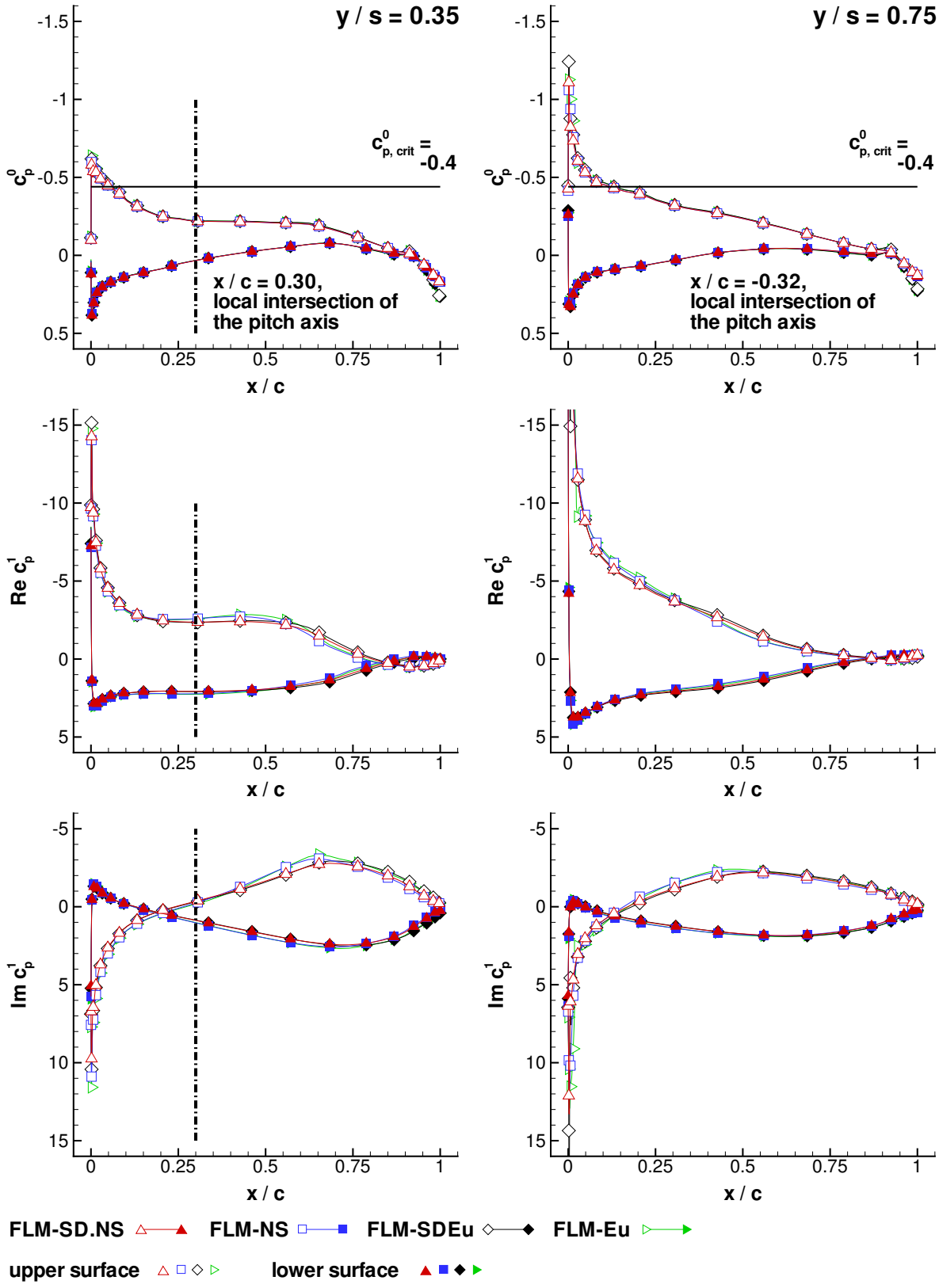


**Fig. 2** Comparison of the zeroth- and first-harmonic pressure-coefficient distributions ($c_p^0$ and $c_p^1$) for the FTDW case P800510 ($Ma_\infty = 0.80$, $Re_\infty = 10.0 \times 10^6$, $\breve{\alpha} = 5.0$ deg, $\breve{\alpha} = 1.0$ deg, $k_{red} = 1.0$, $x_p/c_r = 0.50$)

tribution to the global load-coefficient ($c_L^0$, $Re\,c_L^1$, $Im\,c_L^1$) – across the semispan (Fig. 2). For both $c_L^0$ and $Re\,c_L^1$ the deviation of the inviscid methods is just as negligible as that of the viscous methods before. FLM-SDEu-computed $Im\,c_L^1$, on the other hand, is 5% lower than its FLM-Eu counterpart, though similar to the behavior witnessed between the FLM-SD.NS- and FLM-NS-obtained $Im\,c_L^1$. This implies that the particular deviation is fundamentally inherent to the difference in approach and not to the difference in phenomenological consideration – viscous over inviscid flow.

FLM-SD.NS-rendered $c_M^0$ equals its FLM-NS counterpart. Its marginally negative value (pitch down) indicates that the considered $\breve{\alpha}$ is in close proximity to the incidence angle of zero steady pitching-moment. In contrast to $c_M^0$, FLM-SD.NS-computed $Re\,c_M^1$ and $Im\,c_M^1$ are, respectively, 17% higher and 4% lower in absolute value than the particular FLM-NS-obtained instance. Whereas conformity had been ascertained between the FLM-SD.NS- and FLM-NS-rendered $Re\,c_L^1$, the existing yet negligible deviation has become substantially amplified toward $Re\,c_M^1$. The deviation exhibited in $Im\,c_L^1$, on the other hand, has followed through to $Im\,c_M^1$ unchanged. Since $Re\,c_M^1$ is gained half an order of magnitude smaller than $Im\,c_M^1$, the deviation in $Re\,c_M^1$ itself becomes tolerable. For either method $Re\,c_M^1$ and $Im\,c_M^1$ conform in their negative sign (pitch down), congruently predicting a time-dependent $c_M$ that lags the excitation by slightly more than a quarter cycle: In the case of a free pitching oscillation, $c_M$ would consequently have a damping effect.

Both FLM-SDEu-rendered $c_M^0$ and $Re\,c_M^1$ are 20% higher in absolute value than their viscous counterparts. $Im\,c_M^1$, on the other hand, is rendered merely 6% higher in absolute value. Disregarded viscosity has substantial impact on both $c_M^0$ and $Re\,c_M^1$, despite having had only marginal impact on $c_L^0$ and $Re\,c_L^1$. The relative change of $Im\,c_M^1$, however, remains in-line with the one exhibited by $Im\,c_L^1$. Whereas the disparity in impact witnessed between $c_M^0$ and $c_L^0$ originates from the sensitivity of the $c_M^0$-evaluation for a near zero pitching-moment per se, the one between $Re\,c_M^1$ and $Re\,c_L^1$ stems from $Re\,c_M^1$ being half an order of magnitude smaller than $Im\,c_M^1$. FLM-SDEu-computed $c_M^0$ is 14% lower in absolute value than its FLM-Eu counterpart, as opposed to the observed equality of the viscous instances. Surprisingly, a nearly negligible deviation between the FLM-SDEu- and FLM-Eu-obtained $c_L^0$ amplifies toward a substantial one between the corresponding $c_M^0$ instances. FLM-SDEu-computed $Re\,c_M^1$ and $Im\,c_M^1$ are, respectively, 15% higher and 5% lower in absolute value than their FLM-Eu counterparts. These particular deviations are similar to the ones shown by the corresponding viscous methods, again illustrating that they are fundamentally inherent to the difference in approach. Conforming with the viscous methods, the inviscidly obtained $Re\,c_M^1$ and $Im\,c_M^1$ agree in their negative sign (pitch down). This correspondingly indicates a time-dependent $c_M$ that lags the excitation by slightly more than a quarter cycle. In the case of a free pitching oscillation, $c_M$ would again have a damping effect. The inviscid $Im\,c_M^1$, however, now indicates slightly greater dynamic stability.

Overall, FLM-SD.NS renders the unsteady loading of the shockless case in very good agreement to FLM-NS. For either method the viscous consideration yields both a $c_L^1$- and $c_M^1$-prediction that improves on the respective inviscid approach, yet more distinctly in case of the latter.

## 4.2 Leading-Edge-Vortex Case

For $Ma_\infty = 0.80$, $Re_\infty = 10.0 \times 10^6$, and $\breve{\alpha} = 10.0$ deg the FLM-NS supplied time-invariant mean flowfield exhibits an expanded yet still very localized supersonic region in proximity to the upper wing-surface, originating close to the LE. It extends from $y/s = 0.05$ to $y/s = 0.88$, again terminating without a shock. At $y/s = 0.27$ a vortex additionally initiates close to the upper-surface LE, subsequently convecting toward the tip (Fig. 3). The LEV introduces an extensive region of crossflow to the nearfield. It has developed far greater than the one seen for the

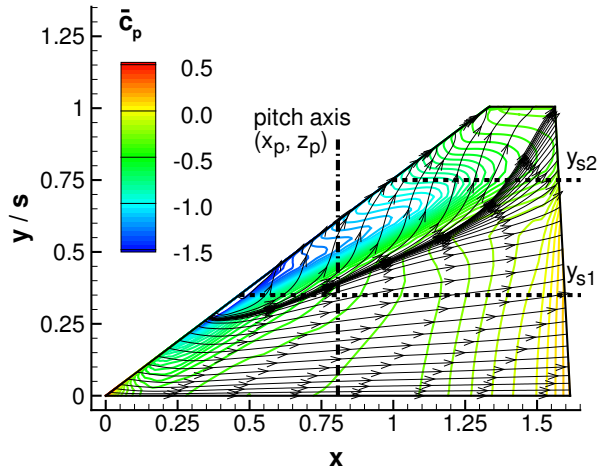


**Fig. 3** Near-surface streamlines and surface isobars of the time-invariant mean flowfield employed by FLM-SD.NS in the FTDW case P801010 ($Ma_\infty = 0.80$, $Re_\infty = 10.0 \times 10^6$, $\breve{\alpha} = 10.0$ deg, $\breve{\alpha} = 1.0$ deg, $k_{red} = 1.0$, $x_p/c_r = 0.50$)

medium-strength-shock/LEV case of the NCDW (90D29) [11]. The LE itself again approximately renders the line of separation, while the line of reattachment is observed at a sweep angle of 66 deg. Over the course of the progression, the LEV initially augments the LE suction-peak, however, to diminishing degree toward $y/s = 0.48$, as it additionally induces a localized suction plateau further downstream. As the LEV's chordwise region of influence expands, the extent of the suction plateau likewise increases, while its intensity decreases in return. In proximity to the tip, the LEV's influence on the surface pressure considerably wanes. With respect to P800510, the additionally rendered rotational component makes for quite the intricate flow topology. FLM-SD.NS-computed surface pressure distributions for P801010 are composited with their FLM-NS and FLM-SDEu / FLM-Eu counterparts in Fig. 4. The characteristic features of the FLM-SD.NS instances are briefly highlighted in the following.

The upper-surface $c_p^0$-progressions exhibit both the precedingly described augmented LE suction-peak and the separately induced suction-plateau, respectively, for the investigated inner- and outer-span station. For the inner-span station, the lower-surface $c_p^0$ progression deviates only slightly from the P800510 instance, despite the substantially higher incidence angle. Contrarily, the outer-span station $c_p^0$ progression indicates strictly expansive flow from the local stagnation point to the TE, where recompression in proximity to the TE had occurred for P800510. Integrating $\Delta c_p^0$ over the entire wing, a positive $c_L^0$ and negative $c_M^0$ (pitch down) can be ascertained.

Naturally, the existence of the LEV and its implied motion alters the upper-surface $Re\,c_p^1$- and $Im\,c_p^1$-progressions as well, however, seen to be less substantial for the inner- than for the outer-span station: The inner-span station instances retain the characteristic features of their P800510 counterparts. Both the $Re\,c_p^1$ minimum-peak and the $Im\,c_p^1$ maximum-peak, which correspond to the location of the $c_p^0$ suction-peak, have diminished in absolute value, yet have increased in chordwise extent. Downstream, however, the progressions again conform to their P800510 counterparts. The lower-surface $Re\,c_p^1$ and $Im\,c_p^1$-progressions mostly conform to their P800510 counterparts as well, with merely the respective peak associated with the location of the stagnation point having faded. For both $Re\,c_p^1$ and $Im\,c_p^1$ the location of the upper- and lower-surface progressions' intersection remains unaltered. Regarding the outer-span station, $Re\,c_p^1$ now exhibits a strictly negative-valued progression. From near the LE toward the half-chord position it can be similarly classified as a plateau. Subsequently, the $Re\,c_p^1$ progression increases toward the TE, equalizing there with the lower-surface instance. The upper-surface $Im\,c_p^1$ progression is similarly negative-valued, yet only up to the half-chord position. From a forward located bulge it monotonically increases to positive values, subsequently intersecting the lower-surface counterpart, and ultimately rendering a local maximum at the three-quarter-chord position. Downstream from there, the $Im\,c_p^1$ progression again increases, equalizing with the lower-surface instance at the TE. With exception of the LE region, the lower-surface $Re\,c_p^1$- and $Im\,c_p^1$-progressions again con-

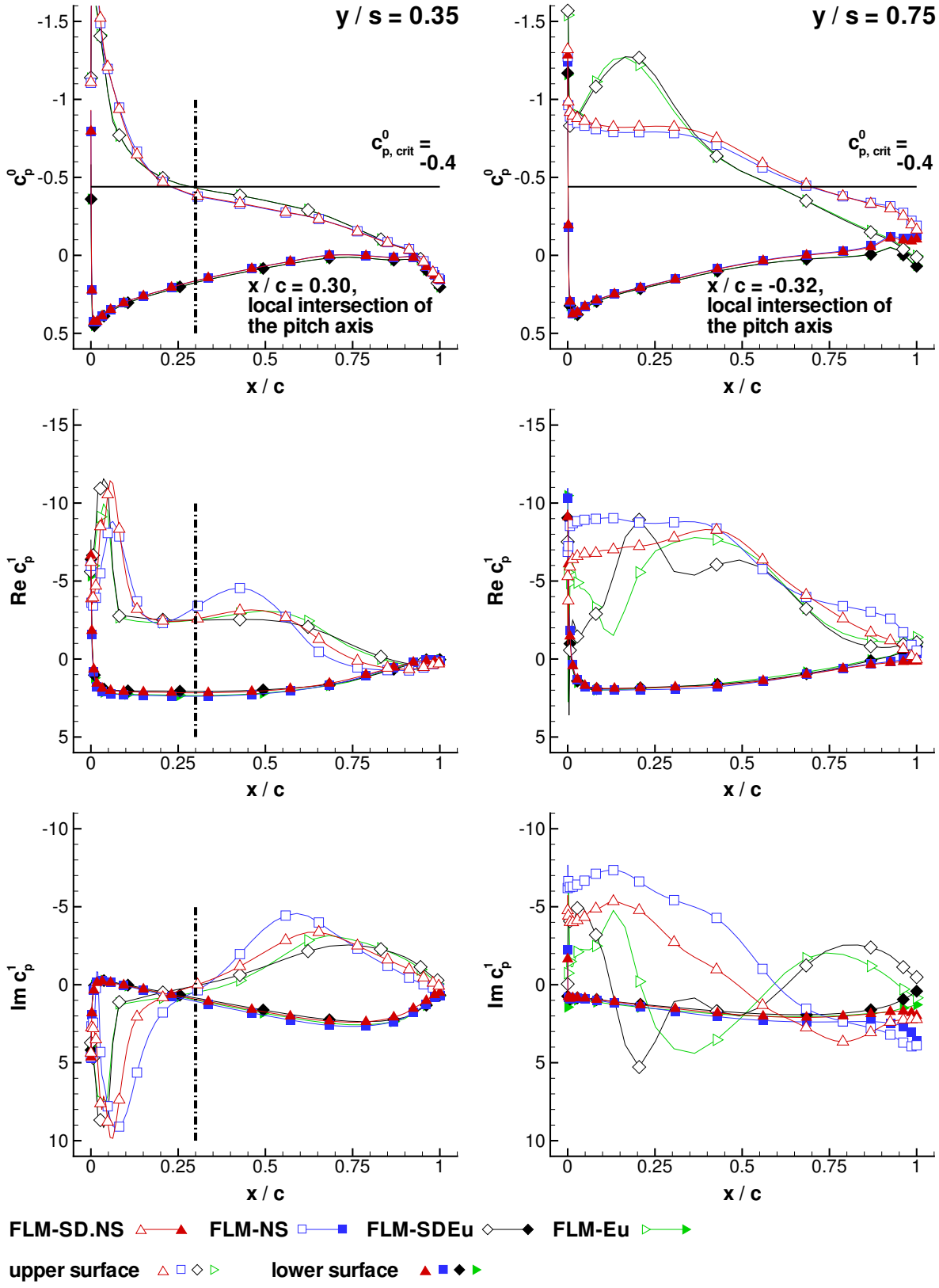


**Fig. 4** Comparison of the zeroth- and first-harmonic pressure-coefficient distributions ($c_p^0$ and $c_p^1$) for the FTDW case P801010 ($Ma_\infty = 0.80$, $Re_\infty = 10.0 \times 10^6$, $\breve{\alpha} = 10.0$ deg, $\breve{\alpha} = 1.0$ deg, $k_{red} = 1.0$, $x_p/c_r = 0.50$)

form to their P800510 counterparts. Integrating $\Delta Re\,c_p^1$, as well as $\Delta Im\,c_p^1$ over the entire wing, respectively, a positive $Re\,c_L^1$ and negative $Re\,c_M^1$ (pitch down), as well as a positive $Im\,c_L^1$ and negative $Im\,c_M^1$ (pitch down), can be ascertained.

FLM-SD.NS-computed upper-surface $c_p^0$ agrees excellently with its FLM-NS-obtained counterpart for the inner-span station, while exhibiting minute discrepancies for the outer-span station with respect to the predicted suction-plateau. For both span stations, greater discrepancies are observed between the FLM-SD.NS-computed upper-surface $Re\,c_p^1$ and its FLM-NS-obtained counterpart, as well as between the corresponding $Im\,c_p^1$ instances. These discrepancies amplify from the inner- toward the outer-span station, in accordance with the LEV's expanding region of influence. Apparently, the small disturbance premise does not hold up well under this circumstance. Agreement between the FLM-SD.NS-computed lower-surface $c_p^0$ and its FLM-NS-obtained counterpart is again excellent, with the corresponding $Re\,c_p^1$ and $Im\,c_p^1$ instances conforming very well likewise.

Equal to the investigation conducted for the NCDW case 90D29, the FLM-SD.NS-computed planform upper-surface $c_p^0$, $c_p^1$ distributions are compared to the planform upper-surface $c_p^0$, $c_p^1$, as well as the planform upper-surface second and third harmonic pressure coefficient distributions ($c_p^2$, $c_p^3$) gained from FLM-NS (Fig. 5 and Fig. 6). Even for a small amplitude of $\breve{\alpha} = 1.0$ deg the imposed motion on the LEV is sufficient to induce higher-order harmonics within the time-dependent evolution of the upper-surface $c_p$. Between the root and the boundary of the LEV's region of influence additional higher-order harmonics emerge about the pitch axis per se, alternating longitudinally in sign. Naturally, both distinct occurrences interact with each other at the boundary of the LEV's region of influence. It can be observed that $c_p^2$ locally exceeds the specified 10% $c_p^1$ range – in parts significantly. In comparison, $c_p^3$ appears fairly subdued with respect to $c_p^1$ as well as to $c_p^2$ . For regions where $c_p^0 \gg c_p^1 \gg c_p^2 \gg c_p^3$ no longer holds true, however, the small disturbance method cannot render an accurate $c_p^1$ prediction: As higher-order harmonics become dominant in the flowfield they exert influence on those of lower order (nonlinear interaction). Consequently, the time-invariant mean flowfield employed by the dynamically linear approach will depart from the actual zeroth-harmonic one. The complex amplitude flowfield computed by FLM-SD.NS can then only deviate from the actual first-harmonic one as well.

Revisiting Fig. 4, the conformity between FLM-SD.NS and FLM-NS can be seen equal to that between FLM-SDEu and FLM-Eu for the upper-surface $c_p^0$-progressions of both span stations. For the inner-span station, the discrepancies between the FLM-SD.NS- and FLM-NS-obtained upper-surface $Re\,c_p^1$ progressions, as well as the $Im\,c_p^1$ instances, are greater than the ones between their inviscid counterparts. For the outer-span station, on the other hand, the FLM-SD.NS- and FLM-NS-obtained upper-surface $Re\,c_p^1$ progressions, as well as the $Im\,c_p^1$ instances, can be ascertained to agree better than their inviscid counterparts. For all lower-surface progressions, conformity between FLM-SD.NS and FLM-NS can again be seen equal to that between FLM-SDEu and FLM-Eu.

Disregarding viscosity has significant impact on the upper-surface progressions, yet almost none on the lower-surface instances. Most notably an upper-surface $c_p^0$ suction-bulge emerges for the outer-span station, where an extended suction-plateau had developed for the viscous treatment. Correspondingly, the inviscid $Re\,c_p^1$ and $Im\,c_p^1$ progressions strongly differ from their viscous counterparts as well. For the inner-span station, however, the inviscidly rendered $c_p^0$-, $Re\,c_p^1$-, and $Im\,c_p^1$-peak at the LE can be observed to be of slightly lesser chordwise extent than their viscous counterparts yet nearly equal in value, despite vortex-initiation being driven by numerical viscosity instead of a physical one.

Regarding the computed global load coefficients (Table 3), $c_L^0$ obtained from FLM-SD.NS can be considered identical to its FLM-NS counterpart. Both $c_L^0$ are nearly two-and-a-half times

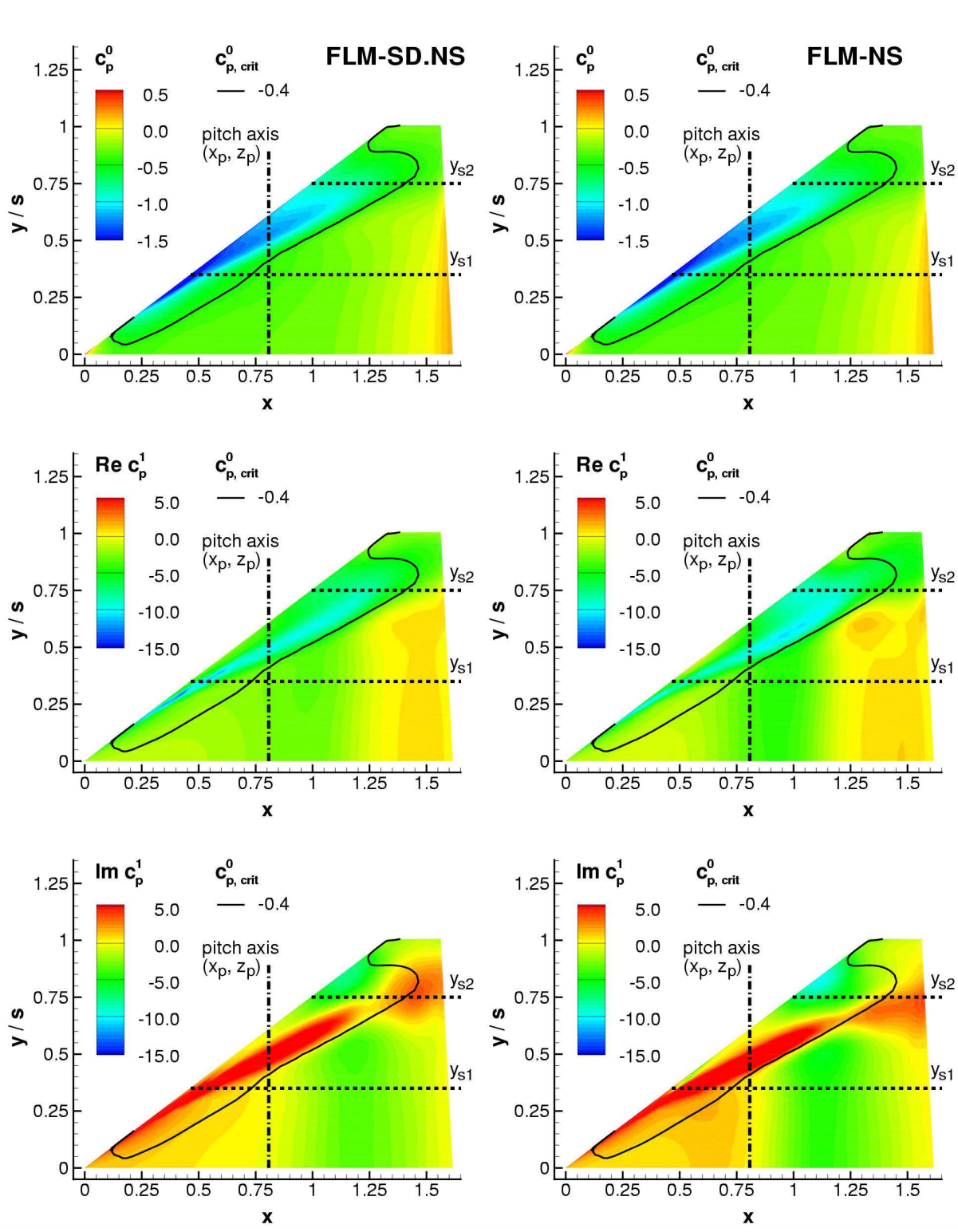


**Fig. 5** FLM-SD.NS- and FLM-NS-computed planform upper-surface $c_p^0$, $c_p^1$ distributions for the FTDW case P801010 ($Ma_\infty = 0.80$, $Re_\infty = 10.0 \times 10^6$, $\breve{\alpha} = 10.0$ deg, $\breve{\alpha} = 1.0$ deg, $k_{red} = 1.0$, $x_p/c_r = 0.50$)

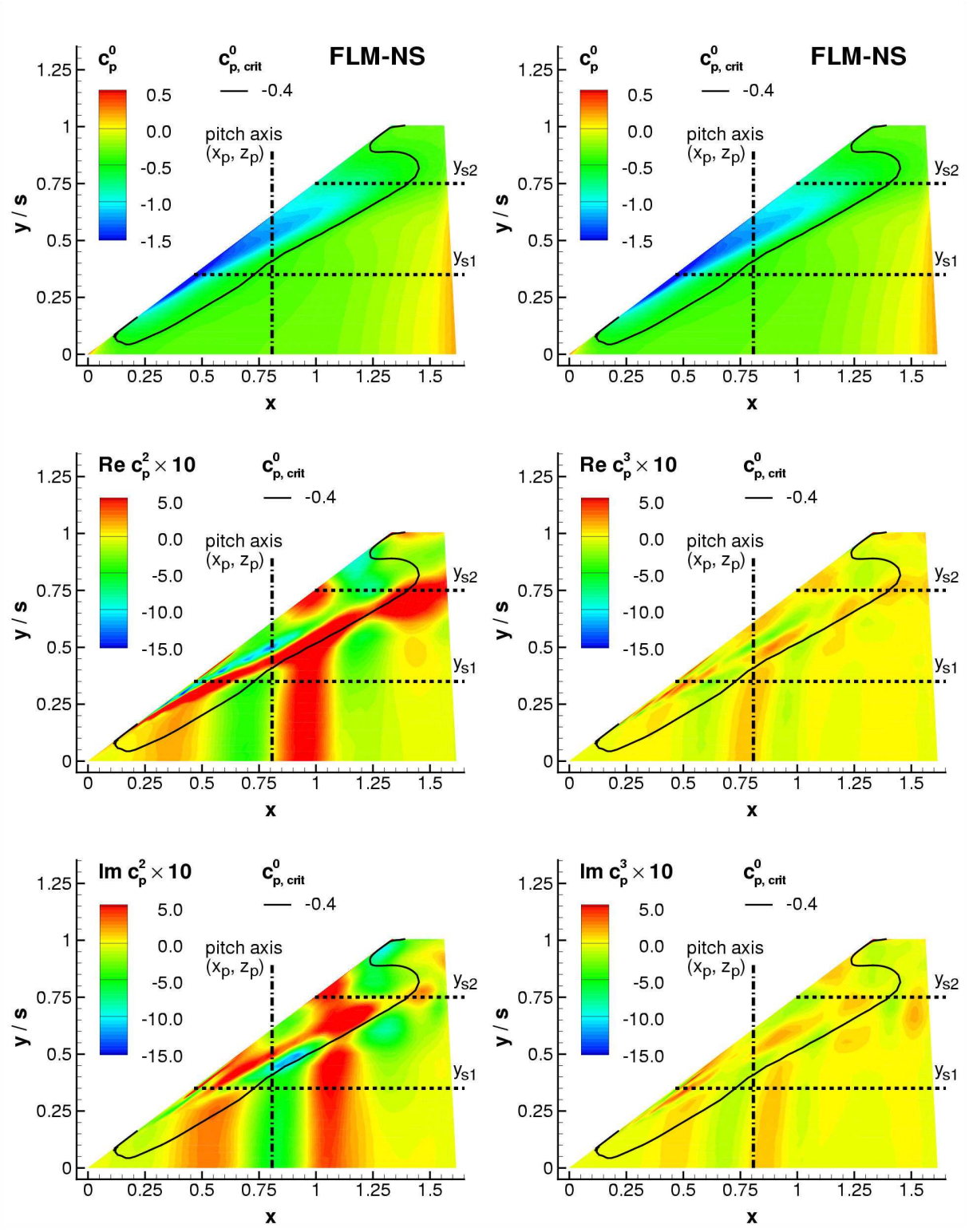


**Fig. 6** FLM-NS-computed planform upper-surface $c_p^0$, $c_p^2$, $c_p^3$ distributions for the FTDW case P801010 ($Ma_\infty = 0.80$, $Re_\infty = 10.0 \times 10^6$, $\breve{\alpha} = 10.0$ deg, $\breve{\alpha} = 1.0$ deg, $k_{red} = 1.0$, $x_p/c_r = 0.50$)

| Method | $c_L^0$ | $Re\,c_L^1$ | $Im\,c_L^1$ |
|---|---|---|---|
| FLM-SD.NS | 0.489 | 4.034 | 1.624 |
| FLM-NS | 0.486 | 4.174 | 1.923 |
| FLM-SDEu | 0.523 | 3.924 | 1.623 |
| FLM-Eu | 0.522 | 3.956 | 1.854 |

| Method | $c_M^0$ | $Re\,c_M^1$ | $Im\,c_M^1$ |
|---|---|---|---|
| FLM-SD.NS | -0.019 | -0.420 | -0.972 |
| FLM-NS | -0.019 | -0.464 | -1.112 |
| FLM-SDEu | -0.034 | -0.464 | -0.996 |
| FLM-Eu | -0.034 | -0.491 | -1.078 |

**Table 3** Comparison of the global load coefficients for FTDW case P801010 ($Ma_\infty = 0.80$, $Re_\infty = 10.0 \times 10^6$, $\breve{\alpha} = 10.0$ deg, $\breve{\alpha} = 1.0$ deg, $k_{red} = 1.0$, $x_p/c_r = 0.50$)

the value exhibited by the viscous instances of case P800510, that is, at equal $Ma_\infty$ yet $\breve{\alpha} = 5.0$ deg. Whereas FLM-SD.NS renders $Re\,c_L^1$ merely 3% lower than the FLM-NS-prediction, $Im\,c_L^1$ is gained 16% lower. Since $Re\,c_L^1$ and $Im\,c_L^1$ are gained in the same order of magnitude, the substantial deviation in $Im\,c_L^1$ cannot be discounted.

FLM-SDEu-rendered $c_L^0$ is 7% higher than its FLM-SD.NS counterpart, attributable to the LEV-induced, and thus highly localized, $c_p^0$ suction-bulge on the upper surface, as exemplified by the outer-span-station progressions (Fig. 4). Integrating over the entire wing, the greater instances of positive $\Delta c_p^0$ eventually yield a greater overall $c_L^0$. In contrast, $Re\,c_L^1$ is gained merely 3% lower than its viscous counterpart, despite the observed disparities between the inviscid and viscous upper-surface $Re\,c_p^1$-progressions in the LEV's region of influence. Obviously, the integration of $\Delta Re\,c_p^1$ over the entire wing toward $Re\,c_L^1$ has had a compensating effect. This behavior is even more evident for $Im\,c_L^1$, having been obtained nearly identical to its viscous counterpart, notwithstanding the illustrated disparity in the $Im\,c_p^1$ progressions. The deviation between the FLM-SDEu- and FLM-Eu-obtained $c_L^0$ is negligible, unlike the one witnessed between the viscous instances. Furthermore, $Re\,c_L^1$ gained from FLM-SDEu is merely 1% lower than its FLM-Eu counterpart, with $Im\,c_L^1$, on the other hand, being 12% lower, notably. Once again, these relative deviations are in line with their respective viscous counterpart, exposing the difference in approach – dynamically fully nonlinear opposite small disturbance – as the cause per se.

FLM-SD.NS-rendered $c_M^0$ equals its FLM-NS counterpart. Its negative value (pitch down) has quadrupled with respect to P800510, placing the considered $\breve{\alpha}$ well beyond the incidence angle of zero steady pitching-moment. In contrast to $c_M^0$, FLM-SD.NS-computed $Re\,c_M^1$ and $Im\,c_M^1$ are, respectively, 10% and 13% lower in absolute value than the particular FLM-NS-obtained instance. Apparently, the small deviation between the FLM-SD.NS- and FLM-NS-rendered $Re\,c_L^1$ has become amplified toward $Re\,c_M^1$, while the substantial deviation exhibited in $Im\,c_L^1$ remains mostly inherent to $Im\,c_M^1$ as well. For either method $Re\,c_M^1$ and $Im\,c_M^1$ conform in their negative sign (pitch down), congruently predicting a time-dependent $c_M$ that lags the excitation by slightly more than a quarter cycle: In the case of a free pitching oscillation, $c_M$ would consequently have a damping effect. For P801010, the degree of dynamic stability is equal to the one seen for P800510, as the mean $Im\,c_M^1$ remains nearly unchanged.

Disregarded viscosity has substantial impact on $c_M^0$, the FLM-SDEu-rendered instance being nearly double its FLM-SD.NS counterpart in negative value (pitch down). Again, this impact can be made attributable to the inviscidly-predicted $c_p^0$ suction-bulge on the upper surface, yet now having to factor in its locality with respect to the pitch axis. Accounting for $\Delta c_p^0$ leverage in this manner, the good agreement between the inner-span-station $c_p^0$ progressions illustrate that the overall sectional contribution to $c_M^0$ is nearly identical for both the FLM-SD.NS and FLM-SDEu instances (Fig. 4). In particular, either method similarly renders an LEV-induced suction-peak in proximity to the LE: Appearing forward of the pitch axis's local intersection, the

sectional contribution of the associated $\Delta c_p^0$ to $c_M^0$ is positive (pitch up), and of nearly equal measure. As the wing is further traversed toward the tip, however, the individual sections no longer intersect the pitch axis beyond $y/s = 0.61$. Being situated aft of the pitch axis, the positive sectional $\Delta c_p^0$ rendered by the pertinent $c_p^0$ progressions of either method thus unambiguously contributes negatively (pitch down) to $c_M^0$. In the inviscid treatment, however, the LEV's initial augmentation of the LE's $c_p^0$ suction-peak evolves into the induction of the separate yet distinct $c_p^0$ suction-bulge. It has greater intensity than the viscously rendered plateau over the course of its existence, as exemplified by Fig. 4. The resultant greater instances of positive $\Delta c_p^0$ produce greater negative sectional contributions (pitch down) to $c_M^0$, eventually amplifying the overall inviscid $c_M^0$ in the integration over the entire wing.

FLM-SDEu-predicted $Re\,c_M^1$ and $Im\,c_M^1$ are, respectively, 10% and 3% higher in absolute value than their FLM-SD.NS-obtained counterparts, with corresponding instances each agreeing in their negative sign (pitch down). Disregarded viscosity impacts $Re\,c_M^1$ more distinctly than $Im\,c_M^1$: Having to factor in leverage with respect to the pitch axis, the apparent disparity between the FLM-SD.NS- and FLM-SDEu-rendered $\Delta Re\,c_p^1$ are compensated less in the integration over the entire wing than the disparity between the corresponding $\Delta Im\,c_p^1$ instances. For either $Re\,c_M^1$ and $Im\,c_M^1$, however, the impact of disregard viscosity amplifies from the behavior observed, respectively, for $Re\,c_L^1$ and $Im\,c_L^1$. FLM-SDEu-obtained $c_M^0$ is equal to its FLM-Eu counterpart, while the $Rec_M^1$ and $Imc_M^1$ instances are, respectively, gained 5% and 8% lower in absolute value. Similar to before, deviations between the FLM-SDEu- and FLM-Eu-rendered $\Delta Re\,c_p^1$, which become quite substantial for the LEV's region of influence (Fig. 4, outer-span station), are compensated slightly less in the integration toward $Rec_M^1$ than $Rec_L^1$. The deviation between the FLM-SDEu- and FLM-Eu-rendered $Imc_M^1$, on the other hand, improves on its $Imc_L^1$ counterpart. All in all, the prediction spread can be considered in-line with the one observed between the inviscid $c_L^0$, $Rec_L^1$, and $Imc_L^1$, as well as within the one exhibited between the viscous $c_M^0$, $Rec_M^1$, and $Imc_M^1$. Again, the later comparison highlights that the deviation witnessed between the viscous methods is fundamentally inherent to the difference in approach. Again, a time-dependent $c_M$ that lags the excitation by slightly more than a quarter cycle is predicted. For a free pitching oscillation, $c_M$ would likewise have a damping effect. As the FLM-SDEu and FLM-Eu rendered $Im\,c_M^1$ both reside within the range established by FLM-SD.NS and FLM-NS, the degree of dynamic stability can be considered to be equal.

Overall, FLM-SD.NS renders the unsteady loading of the LEV case in satisfactory agreement to FLM-NS. For either method, the viscous consideration yields both a $c_L^0$- and $c_M^0$-prediction that substantially improves on the respective inviscid approach. Surprisingly, the viscous consideration improves only marginally on the $c_L^1$- and $c_M^1$-prediction. Relative to P800510 the degree of dynamic stability remains unchanged.

### 4.3 Medium-Strength-Shock Case

For $Ma_\infty = 0.95$, $Re_\infty = 10.0 \times 10^6$, and $\breve{\alpha} = 5.0$ deg the FLM-NS supplied time-invariant mean flowfield exhibits a sizeable supersonic region in proximity to the upper wing surface. It extends from the root to considerably beyond the tip ($y/s \approx 1.60$), initiating closely to the LE and terminating with a medium-strength shock slightly upstream of the TE, across the entire semispan (Fig. 7). Complementarily, a localized supersonic region manifests in proximity to the lower wing surface. It equally extends from the root to considerably beyond the tip, eventually merging with its upper-surface counterpart. At the root, the lower-surface supersonic-region initiates well aft of the half-chord position. As the wing is traversed toward the tip, however, the initiation gradually shifts upstream with respect to the local chord, surpassing the half-chord position beyond $y/s \approx 0.52$, before reaching the LE at the tip itself. The lower supersonic-region is terminated by a weak shock significantly upstream of

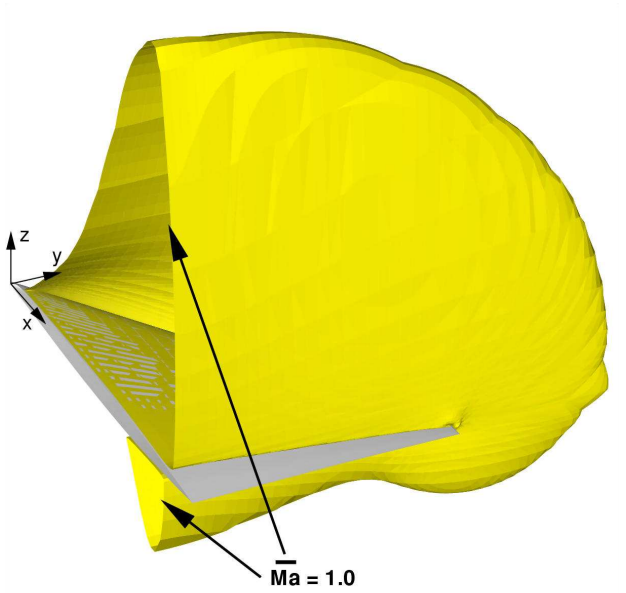


**Fig. 7** Sonic isosurface (aft view) of the time-invariant mean flowfield employed by FLM-SD.NS in the FTDW case P950510 ($Ma_\infty = 0.95$, $Re_\infty = 10.0 \times 10^6$, $\breve{\alpha} = 5.0$ deg, $x_p/c_r = 0.50$, $\breve{\alpha} = 0.5$ deg, $k_{red} = 1.0$)

the TE, across the entire semispan. In this regard, the location of the shock base remains distinctly upstream of its upper-surface counterpart as far as $y/s \approx 0.80$. Beyond, though, the gap between the two instances is quickly narrowed, as the lower-surface shock-base abruptly shifts aft, in order to satisfy upper-surface conformity at the tip. For either shock, the discontinuous recompression is not substantial enough to induce flow separation. FLM-SD.NS-computed surface pressure distributions for P950510 are composited with their FLM-NS and FLM-SDEu / FLM-Eu, counterparts in Fig. 8.

The FLM-SD.NS progressions of P800510 have become modified toward P950510 consistent with a substantially increased region of super-sonic flow on the upper-surface, as well as a newly developed region of super-sonic flow on the lower-surface, and their respective discontinuous termination. Changes in the $c_p^0$ progressions are more prominent for the upper- than the lower-surface. They are of equal distinction, however, in the $Re\,c_p^1$- and $Im\,c_p^1$-progressions. Integrating $\Delta c_p^0$, $\Delta Re\,c_p^1$, as well as $\Delta Im\,c_p^1$ over the entire wing, respectively, a positive $c_L^0$ and negative $c_M^0$, a positive $Re\,c_L^1$ and negative $Re\,c_M^1$ (pitch down), as well as a positive $Im\,c_L^1$ and negative $Im\,c_M^1$ (pitch down), can be ascertained.

For both span stations, FLM-SD.NS-computed $c_p^0$, $Re\,c_p^1$, and $Im\,c_p^1$ agree excellently with those obtained from FLM-NS. The small disturbance premise holds up very well in these near-sonic flow conditions, in part due to the reduced $\breve{\alpha} = 0.5$ deg. Mild discrepancies are merely observed for the lower-surface $Re\,c_p^1$- and $Im\,c_p^1$- progression, respectively, at the location of the weak-shock base and in close proximity to it. The conformity between FLM-SD.NS and FLM-NS can be seen equal to that between FLM-SDEu and FLM-Eu. For disregarded viscosity, merely the location of the medium-strength shock is observed to move somewhat downstream, as rendered by the $c_p^0$ progressions. Correspondingly, a peak uniquely emerges in the inviscid $Re\,c_p^1$-progression where an intersection of the upper- and lower-surface viscous instance is exhibited. The absence of the boundary layer also has an effect on the prediction of the lower-surface $Re\,c_p^1$-peak associated with the weak-shock base. The viscous and inviscid $Im\,c_p^1$ progressions are witnessed to differ even more marginally for these occurrences. In terms of the time domain, either treatment renders a nearly stationary medium-strength-shock over the course of the individual cycle, with the weak shock exhibiting a distinct longitudinal motion.

Focusing on the computed global load coefficients (Table 4), $c_L^0$ obtained from FLM-SD.NS is identical to its FLM-NS counterpart. Both $c_L^0$ are 22% higher than the value exhibited by the viscous instances of case P800510, that is, at equal $\breve{\alpha}$ yet $Ma_\infty = 0.8$. Similar to P800510, the deviation between the FLM-SD.NS- and FLM-NS-obtained $Re\,c_L^1$ is negligible, while the FLM-SD.NS prediction of $Im\,c_L^1$ is 7% higher than its FLM-NS counterpart. Once again, $Re\,c_L^1$ and $Im\,c_L^1$ are gained in the same order of magnitude. Both computations indicate a time-dependent $c_L$

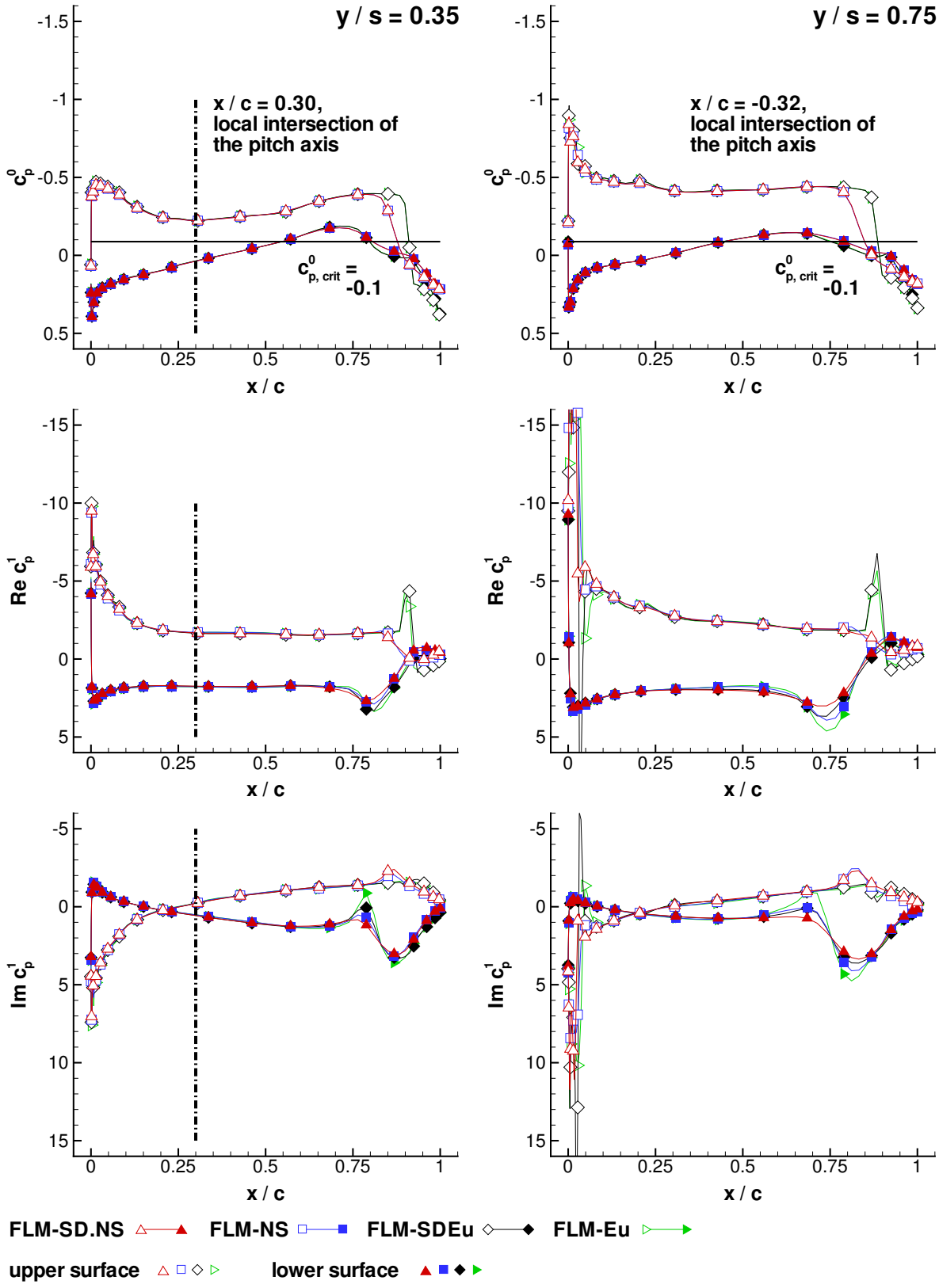


**Fig. 8** Comparison of the zeroth- and first-harmonic pressure-coefficient distributions ($c_p^0$ and $c_p^1$) for the FTDW case P950510 ($Ma_\infty = 0.95$, $Re_\infty = 10.0 \times 10^6$, $\breve{\alpha} = 5.0$ deg, $\hat{\alpha} = 0.5$ deg, $k_{red} = 1.0$, $x_p/c_r = 0.50$)

| Method | $c_L^0$ | $Re\,c_L^1$ | $Im\,c_L^1$ |
|---|---|---|---|
| FLM-SD.NS | 0.260 | 3.565 | 1.192 |
| FLM-NS | 0.260 | 3.579 | 1.114 |
| FLM-SDEu | 0.281 | 3.780 | 1.167 |
| FLM-Eu | 0.281 | 3.775 | 1.114 |

| Method | $c_M^0$ | $Re\,c_M^1$ | $Im\,c_M^1$ |
|---|---|---|---|
| FLM-SD.NS | -0.027 | -0.571 | -0.779 |
| FLM-NS | -0.027 | -0.580 | -0.743 |
| FLM-SDEu | -0.038 | -0.696 | -0.771 |
| FLM-Eu | -0.038 | -0.690 | -0.751 |

**Table 4** Comparison of the global load coefficients for FTDW case P950510 ($Ma_\infty = 0.95$, $Re_\infty = 10.0 \times 10^6$, $\breve{\alpha} = 5.0$ deg, $\hat{\alpha} = 0.5$ deg, $k_{red} = 1.0$, $x_p/c_r = 0.50$)

that distinctly leads the excitation. With the wing predominantly enveloped by supersonic flow, a time-dependent $c_L$ of notably lesser amplitude and significantly lesser lead to the excitation is rendered than in case of prevalent subsonic flow.

FLM-SDEu-rendered $c_L^0$ is 8% higher than its FLM-SD.NS counterpart: As illustrated by both the inner- and outer-span-station $c_p^0$-progressions (Fig. 8), across the semispan the medium-strength shock is situated farther aft in absence of the boundary layer. The location of the weak lower-surface shock, on the other hand, remains all but unchanged. Together, greater instances of positive $\Delta c_p^0$ are gained, which eventually yield a greater overall $c_L^0$ in the integration over the entire wing. Disregarded viscosity effects $Re\,c_L^1$ in similar fashion: Associated with the medium-strength shock, the otherwise nonexistent upper-surface $Re\,c_p^1$-peak is primarily responsible for producing greater instances of positive $\Delta Re\,c_p^1$ across the semispan. The limited disparity emerging between the inviscid and viscous prediction of the lower-surface $Re\,c_p^1$-peak, as associated with the weak-shock base, increases the positive $\Delta Re\,c_p^1$ only marginally. Overall, $Re\,c_L^1$ is rendered 6% higher in return. Disregarded viscosity effects $Im\,c_L^1$ even less, with the FLM-SDEu-rendered instance being merely 2% lower than its FLM-SD.NS counterpart: Contributing deviations in the particular $Im\,c_p^1$-progressions are primarily seen to occur on the lower-surface, that is, for the local minimum associated with the weak-shock base, as well as for the subsequent peak of the post-shock region. FLM-SDEu- and FLM-Eu-obtained $c_L^0$ are identical, while the deviation between the two $Re\,c_L^1$ instances can be considered negligible, just as ascertained for the viscous counterparts precedingly. FLM-SDEu-computed $Im\,c_L^1$, on the other hand, is 5% higher than its FLM-Eu counterpart, though again within the spread established by FLM-SD.NS and FLM-NS before. With similar behavior already ascertained for both P800510 and P801010, it can be considered substantiated that the particular viscous deviation mainly originates from the difference in approach, and not the greater complexity of the utilized flow model.

FLM-SD.NS-rendered $c_M^0$ equals its FLM-NS counterpart. With respect to P800510, the near-sonic $Ma_\infty$ has amplified $c_M^0$ in its negative value fivefold, again placing the considered $\breve{\alpha}$ well beyond the incidence angle of zero steady pitching-moment. In contrast to $c_M^0$, FLM-SD.NS-computed $Re\,c_M^1$ and $Im\,c_M^1$ are, respectively, 2% lower and 5% higher in absolute value than the particular FLM-NS-obtained instance. Whereas near-identity had been ascertained between the FLM-SD.NS- and FLM-NS-rendered $Re\,c_L^1$, the existing yet negligible deviation has become distinctly amplified toward $Re\,c_M^1$. The deviation exhibited in $Im\,c_L^1$, on the other hand, has become slightly mitigated toward $Im\,c_M^1$. For either method $Re\,c_M^1$ and $Im\,c_M^1$ conform in their negative sign (pitch down), congruently predicting a time-dependent $c_M$ that lags the excitation by nearly three-eights of a cycle. In the case of a free pitching oscillation, $c_M$ would consequently have a damping effect. In accordance with the $\hat{\alpha}$-normalized instance of Eq. (4) in [11], $\left|Im\,c_M^1\hat{\alpha}\right|_{P950510} < \left|Im\,c_M^1\hat{\alpha}\right|_{P800510}$ can be established for the mean $Im\,c_M^1$. Thus, for P950510 $\tilde{c}_M$ extracts 60% less systemic energy with respect

to $\tilde{\alpha}$ than for P800510, signifying a substantially lesser degree of dynamic stability.

FLM-SDEu-rendered $c_M^0$ and $Re\,c_M^1$ are, respectively, 41% and 22% higher in absolute value than the particular FLM-SD.NS-obtained instance. $Im\,c_M^1$, on the other hand, is rendered merely 1% lower in absolute value, allowing it to be considered equal to its viscous counterpart. FLM-SDEu-rendered $c_M^0$, $Re\,c_M^1$, and $Im\,c_M^1$ each agree in their negative sign (pitch down) with the particular FLM-SD.NS-obtained instance. $Re\,c_M^1$ and $Im\,c_M^1$ are not only again in the same order of magnitude, but are separated by merely 10% in actual value. Disregarded viscosity has a substantial impact on both $c_M^0$ and $Re\,c_M^1$, despite having had only minor impact on $c_L^0$ and $Re\,c_L^1$. The relative change of $Im\,c_M^1$, however, remains in-line with the one exhibited by $Im\,c_L^1$. The disparity in impact witnessed between $c_M^0$ and $c_L^0$, as well as between $Re\,c_M^1$ and $Re\,c_L^1$, again results from accounting $\Delta c_p^0$- and $\Delta Re\,c_p^1$-leverage, respectively, with regard to the pitch axis: As illustrated in Fig. 8 for the inner- and outer-span station, the FLM-SD.NS and FLM-SDEu instances of the $c_p^0$ progression, as well as the $Re\,c_p^1$ progression, mostly conform to each other, with the inviscidly predicted location of the medium-strength shock and the upper- and lower-surface shock-peaks being the exception. The locality of the additional positive $\Delta c_p^0$ and positive $\Delta Re\,c_p^1$ generated by these occurrences is unambiguously situated far aft of the pitch axis. Hence, the extra sectional-contribution to $c_M^0$ and $Re\,c_M^1$ is always substantially negative (pitch down), eventually amplifying the overall instances in the integration over the entire wing. FLM-SDEu-obtained $c_M^0$ is equal to its FLM-Eu counterpart, while the deviation between the $Re\,c_M^1$ instances is marginal. Furthermore, FLM-SDEu renders $Im\,c_M^1$ merely 3% higher in absolute value than FLM-Eu. Consequently, the prediction spread lies within the one observed between the inviscid $c_L^0$, $Re\,c_L^1$, and $Im\,c_L^1$ instances, as well as within the one exhibited between the viscous $c_M^0$, $Re\,c_M^1$, and $Im\,c_M^1$ instances. Once more, the latter comparison substantiates that the deviation witnessed between the viscous methods is fundamentally inherent to the difference in approach. Again, a time-dependent $c_M$ that lags the excitation by nearly three-eights of a cycle is predicted. In the case of a free pitching oscillation, $c_M$ would likewise have a damping effect. Nevertheless, as the FLM-SDEu and FLM-Eu rendered $Im\,c_M^1$ both reside within the range established by FLM-SD.NS and FLM-NS, the degree of dynamic stability can be considered to be equal.

Overall, FLM-SD.NS renders the unsteady loading of the shockless case in very good agreement to FLM-NS. For either method the viscous consideration yields both a $c_L^0$- and $c_M^0$-prediction that substantially improves on the respective inviscid approach. The viscous consideration improves on both the $c_L^1$- and $c_M^1$-prediction as well, however, to a significantly lesser extent. Relative to P800510 the degree of dynamic stability is greatly reduced.

## 5 Computational Efficiency

FLM-SD.NS and FLM-NS computation times, as well as the inverse ratio between the two are summarized for the production cases in Tab. 5. Evidently, FLM-SD.NS realizes reductions up to half an order of magnitude. At its least, that is, for case P950510, however, $\check{t}_{CPU}^{SD.NS}$ is gained merely 37% lower than $\check{t}_{CPU}^{NS}$: Despite having employed a computational grid-pair which is equal in cell number to the baseline grid-pair of the NCDW investigations, as well as the same processor, $\check{t}_{CPU}^{SD.NS}$ is gained greater than the established 24 h reference time frame [11]. Inversely, $\check{t}_{CPU}^{NS}$ is gained substantially lower than for the NCDW shock cases, attributable to the exceptional convergence behavior of the dual-time-stepping scheme exhibited for P950510.

## 6 Conclusions

In an effort to complement past investigations on the unsteady aerodynamic loading of a FTDW undergoing harmonic motions, results for rigid-body pitching-oscillations computed with FLM-SD.NS were presented and compared to those of FLM-NS, as well as FLM-SDEu / FLM-Eu.

| Case | $\check{t}_{CPU}^{SD.NS}$, h | $\check{t}_{CPU}^{NS}$, h | $\zeta_{CPU}$ |
|---|---|---|---|
| P800510 | 20.7 | 71.4 | 3.4 |
| P801010 | 40.1 | 94.3 | 2.4 |
| P950510 | 32.5 | 51.8 | 1.6 |

**Table 5** Comparison of computational effort between FLM-SD.NS and FLM-NS for the FTDW cases as realized on the Intel Itanium 2 (1.3 GHz)

A shockless case, serving as baseline, and a medium-strength-shock case again demonstrated the small disturbance Navier-Stokes approach's accuracy in predicting the unsteady local and global loading. Similarly, the LEV case disclosed the known limitations of the small disturbance approach. However, deviations caused by flow-inherent higher-harmonics are observed to be far less severe than exhibited for the medium-strength-shock/LEV case of the NCDW. Surprisingly, the degree of dynamic stability ascertained for the FTDW's LEV case can be considered equal to its baseline-case instance, despite featuring substantially differing upper-surface-proximate flowfields – a mixed translational/rotational one versus a strictly translational one. In contrast, the degree of dynamic stability ascertained for the FTDW's medium-strength-shock case emerges greatly reduced with respect to its baseline counterpart – a wing predominantly enveloped by supersonic flow versus subsonic flow apparently being the more profound topological shift.

For all cases, the comparison between the viscous and inviscid surface-pressure distributions shows that the impact of the boundary-layer is severely limited for regions of strictly longitudinal flow, as subject to expansion and continuous recompression. For both the LEV and medium-strength-shock case, however, disregarding viscosity distinctly alters the upper-surface pressure distributions outside of these regions, naturally following through to the global loading as well. Especially, the case particular inviscid $c_L^0$- and $c_M^0$-prediction are observed to substantially differ from their viscous counterparts, while the $c_L^1$- and $c_M^1$-prediction, surprisingly, are impacted to a lesser extent. Consequently, the viscous consideration improves on the merely inviscid one per se. For each case, however, the degree of dynamic stability determined with FLM-SDEu / FLM-Eu is quite similar to the FLM-SD.NS / FLM-NS-assessed counterpart. The comparison between the viscous and inviscid global load coefficients further revealed that the relative deviation exhibited by the FLM-SD.NS- and FLM-NS-obtained instances is in part already inherent to the FLM-SDEu- and FLM-Eu-predictions.

With exception of the FTDW's medium-strength-shock case, FLM-SD.NS efficiency gain over FLM-NS is substantial, however, significantly less than exhibited for the NCDW cases. This circumstance is attributable to the much shorter computational time required by FLM-NS to render the FTDW cases.

All in all, FLM-SD.NS remains the CFD method of choice for predicting unsteady aerodynamic structural loading efficiently as well as accurately in the transonic flow regime. To this effect, the investigated FTDW cases have illustrated that both the reduction of computational cost and the need to actually consider viscosity is greatly case-dependent, and typically not a priori known.

## 7 Acknowledgments

The author would like to thank Prof. em. Dr.-Ing. Boris Laschka for his counsel and support over many years. The author also expresses his gratitude toward the Institute of Aerodynamics and Fluid Mechanics for having continuously provided office space and infrastructure access.

## References

[1] Bennett, R. M., and Walker, C. E. Computational test cases for a clipped delta wing with pitching and trailing edge control surface oscillations. NASA TM-1999-209104, 1999.

[2] Dufour, G., Sicot, F., Puigt, G., Liauzun, C., and Dugeai, A. Contrasting the harmonic balance and linearized methods for oscillating-flap sim-

ulations. *AIAA Journal*, Vol. 48, No 4, pp 788–797, 2010.

[3] Iatrou, M. Ein Navier-Stokes-Verfahren kleiner Störungen für instationäre Vorgänge - Anwendung auf Transportflugzeuge. Ph.D. Dissertation, Institute of Aerodynamics, Technische Universität München, Garching, Germany, Nov. 2009.

[4] Iatrou, M., Allen, A., Pechloff, A., Breitsamter, C., and Laschka, B. Small disturbance Euler/Navier-Stokes computations for delta wing flap oscillations. *Proc Flow-Induced Unsteady Loads and the Impact on Military Applications*, pp 16–1–16–12, RTO-MP-AVT-123, Budapest, Hungary, April 2005.

[5] Kreiselmaier, E., and Laschka, B. Small disturbance Euler equations: Efficient and accurate tool for unsteady load predictions. *Journal of Aircraft*, Vol. 37, No 5, pp 770–778, 2000.

[6] Levasseur, V., Chalot, F., Daumas, L., and Forestier, N. Harmonic aerodynamics loads prediction including a linerized turbulence model. IFASD Paper 2011-129, Paris, June 2011.

[7] Liauzun, C., Canonne, E., and Mortchéléwicz, G. D. Flutter numerical computations using the linearized Navier-Stokes equations. *Proc Advanced Methods in Aeroelasticity*, pp 8–1–8–12, RTO-MP-AVT-154, Loen, Norway, May 2008.

[8] Markmiller, J. Validierung eines zeitechten und eines small disturbance Navier-Stokes Verfahrens an einem schwingenden Deltaflügel. Diploma Thesis TUM-FLM-2003/28, Aerodynamics Division, Institute for Fluid Mechanics, Technische Universität München, Garching, Germany, Oct. 2003.

[9] Pechloff, A., and Laschka, B. Small disturbance Navier-Stokes method: Efficient tool for predicting unsteady air loads. *Journal of Aircraft*, Vol. 43, No 1, pp 17–29, 2006.

[10] Pechloff, A., and Laschka, B. Small disturbance Navier-Stokes computations employing the Wilcox k-omega turbulence model. 27th Congress of the International Council of the Aeronautical Sciences, ICAS Paper 2010-3.10.5, Nice, France, Sep. 2010.

[11] Pechloff, A., and Laschka, B. Small disturbance Navier-Stokes computations for low-aspect-ratio wing pitching oscillations. *Journal of Aircraft*, Vol. 47, No 3, pp 737–753, 2010.

[12] Revalor, Y., Daumas, L., and Forestier, N. Industrial use of CFD for loads and aero-servo-elastic stability computations at Dassault Aviation. IFASD Paper 2011-061, Paris, June 2011.

[13] Schuster, D. M., Liu, D. D., and Huttsell, L. J. Computational aeroelasticity: Success, progress, challenge. *Journal of Aircraft*, Vol. 40, No 5, pp 843–856, 2003.

[14] Sickmüller, U. Luftkräfte höherer Ordnung auf Basis der Euler Gleichungen bei kleinen Störungen. Ph.D. Dissertation, Institute of Aerodynamics, Technische Universität München, Garching, Germany, Nov. 2005.

[15] Spalart, P. R., and Allmaras, S. R. A one-equation turbulence model for aerodynamic flows. AIAA Paper 92-0439, Jan. 1992.

[16] Weishäupl, C., and Laschka, B. Small disturbance Euler simulations for delta wing unsteady flows due to harmonic oscillations. *Journal of Aircraft*, Vol. 41, No 4, pp 782–789, 2004.

[17] Widhalm, M., Dwight, R. M., Thormann, R., and Hübner, A. Efficient computation of dynamic stability data with a linearized frequency domain solver. *Proc V European Conference on Computational Fluid Dynamics*, ECCOMAS CFD 2010, Lisbon, Portugal, 2010.